

Assessing the feasibility of process window estimation for L-PBF Ti-6Al-4V through hardness measurements

Arun Poudel, Mohammad Salman Yasin, Shuai Shao, Nima Shamsaei*

National Center for Additive Manufacturing Excellence (NCAME), Auburn University, Auburn,
AL 36849, USA

Department of Mechanical Engineering, Auburn University, Auburn, AL 36849, USA

* Corresponding author: shamsaei@auburn.edu

Phone: (334) 844-4839

Abstract

Optimizing the process window for an additively manufactured material using X-ray computed tomography (XCT) is a time-, labor-, and capital-intensive process where a large number of coupons need to be analyzed in the process parameter space. Hence, as a cheaper and faster alternative, this study assessed the relationship between relative density and hardness of laser powder bed fused (L-PBF) Ti-6Al-4V. Coupons with different levels of porosity were fabricated by changing the recommended laser power in the range of $\pm 20\%$ in an interval of 10%. The martensitic microstructure didn't vary significantly with the change in laser power. On the other hand, Rockwell C hardness (HRC) did. HRC was observed to be in good correlation with the defect content in the coupons. Higher defect content in the coupons resulted in lower HRC and vice versa. Hence, the hardness measurement technique can be used to estimate the process window of L-PBF Ti-6Al-4V.

Keywords: Laser powder bed fusion (L-PBF), Non-destructive testing, X-ray computed tomography, Process window, Rockwell hardness

Introduction

One of the major distinctions that separate the additively manufactured (AM) parts from the conventionally manufactured ones is the presence of a higher number of volumetric defects [1,2]. During loading, these defects act as stress risers and can deteriorate both tensile properties as well as fatigue performance of AM parts [3–6]. Generally, post-fabrication treatment such as hot isostatic pressing (HIP) is implemented to reduce the degree of porosity and its influence on the mechanical performance [7–12]. However, the complete removal of entrapped pores, as well as large-sized defects from AM parts, is difficult [4,13–15] if not impossible. Another way to improve the mechanical properties, especially fatigue, of AM parts is to minimize their formation during the AM process.

To minimize defect formation, AM parts are fabricated utilizing a predetermined set of process parameters such as laser power, laser speed, hatch distance, etc., residing well within the process window for a specific material and AM process [16]. Typically, a process window is established based on the relative density of the parts fabricated using different process parameters [17–20]. Relative density is typically measured using different techniques such as Archimedes, X-ray computed tomography (XCT), micrography of cross sections, etc. [21,22]. Among these

techniques, the high-resolution XCT has been observed to estimate the density and characterize the defects in the AM parts with good accuracy [22,23].

The XCT is an advanced imaging technique that utilizes an X-ray beam to detect the voids and foreign particles in a body/part [24]. Even though XCT is an accurate nondestructive evaluation (NDE) technique, its results are highly dependent on the voxel size used during the scans. The use of different voxel sizes has been observed to result in different defect information even for the same part [25]. Furthermore, performing an XCT scan and post processing the data is a time-and capital-intensive process. The emergence of new AM materials as well as techniques demands a fast and relatively robust approach to establish the process window. In this regard, considering the microstructure of the material is constant, the hardness has been observed to correlate well with the porosity level [26,27]. Hence, hardness measurements can be considered an appealing alternative to assess the porosity and estimate the process window for AM materials [28,29].

Few studies have been done to investigate the hardness of AM materials fabricated using different process parameters [26,27]. However, a thorough investigation correlating the porosity with the hardness of the AM material is still lacking. Hence, this study fabricated the coupons by altering the laser power from manufacturer recommended process parameters and obtained the process window via both XCT and Rockwell C hardness (HRC) measurements. This assessed the feasibility of process window estimation for laser powder bed fused (L-PBF) Ti-6Al-4V Grade 5 material using the hardness measurements.

Material and methods

Plasma atomized Ti-6Al-4V Grade 5 powder supplied by Advanced Powders and Coating (AP&C) with a size distribution in the range of 15 μm to 53 μm was used to fabricate coupons using EOS M290, a laser powder bed fusion (L-PBF) AM machine. The chemical composition of the feedstock powder as provided by the manufacturer is shown in **Table 1**. Different level of porosity was induced by altering the recommended laser power from +20% to -20% in the intervals of 10% (i.e., P^{+20%}, P^{+10%}, P^{0%}, P^{-10%}, and P^{-20%}). The coupons were named P^{x%} which suggests that the laser power was changed by x% during its fabrication with all other process parameters remaining constant. The EOS recommended process parameters for Ti-6Al-4V Grade 5 material include 280 W laser power, 1200 mm/sec laser speed, 30 μm layer thickness, 140 μm hatch distance, 67° inter-layer rotation, and 10 mm stripe width. The geometry and dimensions of the coupons used for XCT and hardness tests are shown in **Fig. 1**. The XCT scans were performed using ZEISS Xradia 620 Versa machine and hardness tests using the LECO LCR-500 HRC tester.

Table. 1 Chemical composition of the Ti-6Al-4V grade 5 powder provided by AP&C [30].

	Al	V	Fe	O	C	N	H	Y	Ti
Wt. %	6.260	3.910	0.210	0.140	0.010	0.010	0.002	<0.001	Bal.

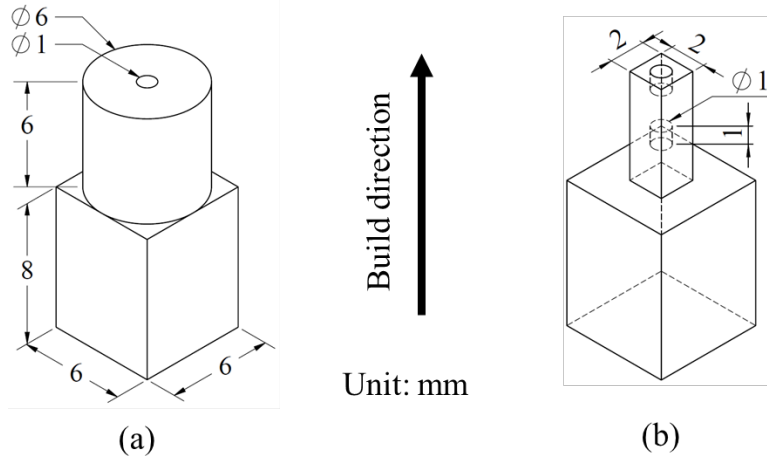


Fig. 1 Geometry and dimension of L-PBF Ti-6Al-4V coupon in (a) as-built and (b) machined conditions.

The hardness tests were performed in accordance with ASTM E18-20 [31]. For hardness tests, the as-built coupons (see **Fig. 1(a)**) were mounted in a cold set epoxy resin and polished using sandpapers with grit sizes ranging from P280 to P360. Furthermore, it was polished from both sides to make the coupons flat as well as to let hardness coupons touch the tester platform. Eight indents were made using a diamond spheroconical indenter in the transverse plane; i.e., perpendicular to the build direction in the top cylindrical portion of every coupon. According to ASTM E18-20, a 150kgf total test force was applied for each indentation. The microstructural analysis of these coupons was performed using Zeiss 550 scanning electron microscope equipped with a back-scatter electron (BSE) detector. Similar to the hardness tests, the BSE imaging was performed on the transverse plane. Regarding XCT, the coupons were machined to a geometry seen in **Fig. 1(b)**. The smaller-sized coupon enables the high-resolution scans (i.e., voxel size of 1 μm) in its center. The scans were performed using 160 kV voltage and 25 W power X-ray source. After the scan, the reconstructed absorption data were post-processed using Dragonfly and ImageJ software [32,33] to calculate the relative density of the fabricated coupons.

Results and discussion

Process window obtained via XCT

Different level of porosity was induced in coupons fabricated by altering the laser power as seen in **Fig. 2**. The underheated (i.e., laser power lower than recommended) coupons mostly consisted of irregularly shaped lack of fusions (LoFs), while overheated (i.e., laser power higher than recommended) ones had small-sized gas-entrapped pores (GEPs). The size and number of defects in the underheated coupons increased with a decrease in the laser power during the fabrication process. In the case of P^{0%} coupon, small-sized spherical defects and one irregular-shaped defect, shown using a green arrow in **Fig. 2** were observed. The levels of porosity in recommended and overheated ones seemed to be similar. No keyholes (KHs) were observed in the overheated coupons. The volume of the defects observed in **Fig. 2** was quantified and the relative density of the coupons is presented in **Fig. 3**. According to the observation made using **Fig. 2**, the relative density of the underheated coupons decreased with decreasing energy inputs during the fabrication process. In addition, the relative densities of the recommended and overheated coupons

were observed to be approximately equal. It was attributed to the sufficient melt-pool overlaps in between the adjacent laser track as well as layers—prevents the formation of LoFs—and also, not enough energy to induce KHs.



Fig. 2 Visualization of defects induced in coupons fabricated using different laser power. The green arrow points toward an irregular-shaped defect, most likely an LoF in $P^{0\%}$ coupon. The scale bar corresponds to all coupons.

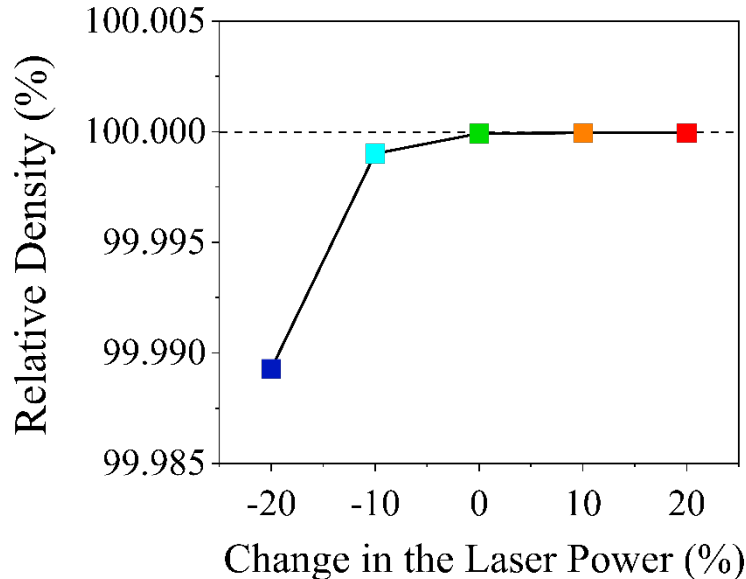


Fig. 3 Relative density of coupons fabricated using different laser power.

Process window obtained via hardness measurements

The HRC of the Ti-6Al-4V coupons fabricated by different laser power is shown using a box plot in **Fig. 4**. The HRC was observed to follow a similar trend as the part density of the coupons as seen in **Fig. 3**. The average HRC of the recommended coupon was the highest among the considered coupons. In underheated coupons (i.e., $P^{-10\%}$ and $P^{-20\%}$), the mean of the HRC decreased and its range increased with the decrease in the energy input. In other words, the HRC values decreased with the increase in the defect content in the underheated coupons. Similarly, in the case of overheated coupons (i.e., $P^{+10\%}$ and $P^{+20\%}$), the absence of defects led to similar HRC values as recommended ones. **Fig. 4** illustrates a significant overlap in the range of HRC between recommended and overheated coupons. It is in agreement with the density measurements performed via XCT.

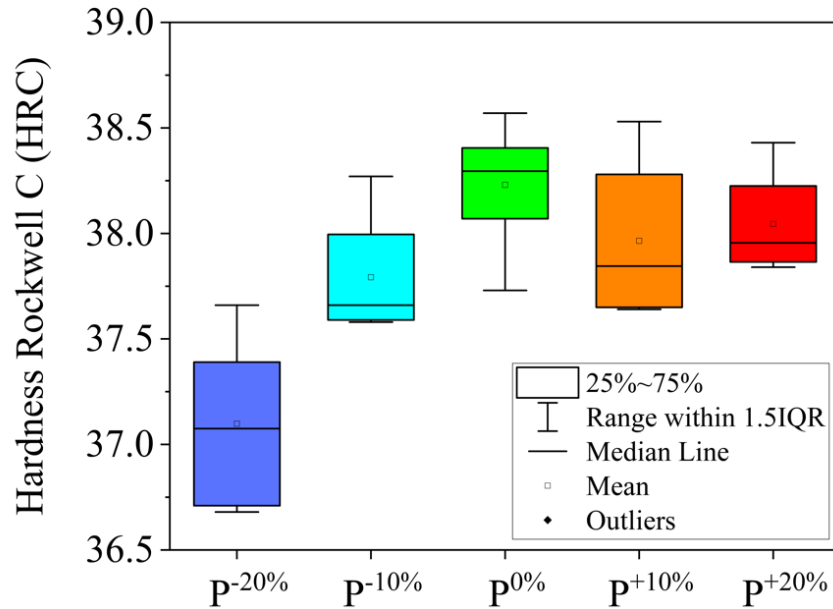


Fig. 4 Comparison of HRC among the coupons fabricated using altered laser power. In the legend, IQR denotes the interquartile range.

In order to understand the role of microstructure on the hardness of the fabricated coupons, BSE imaging was performed and the resulting images are shown in **Fig. 5**. The martensitic microstructure was observed in all the coupons. The lath thickness did not vary significantly with the variation in the laser power used during fabrication. The hardness of Ti-6Al-4V material is dependent on the grain size [27]. The hardness value decreases with the increase in the grain size and vice versa. The similarity in the microstructure of the coupons fabricated using different laser power (see **Fig. 5**) suggests its minimal influence on the variation of their hardness values as shown in **Fig. 4**. Hence, the variation in the hardness values was attributed to the defect content in the coupons. As seen in **Fig. 2**, the increase in the defect content in the underheated coupons resulted in their lower hardness. In addition, the increase in the number and size of the defects in P^{-20%} coupon as compared to P^{-10%} has increased the range of variation in their hardness values. On the other hand, the overheated and P^{0%} coupons have similar hardness values due to the similar level of defect content (see **Fig. 2**).

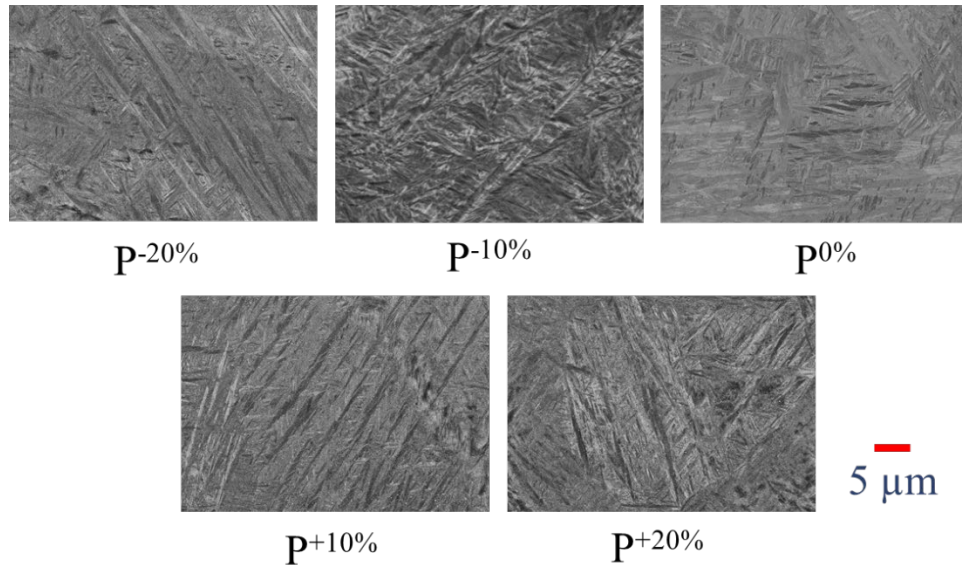


Fig. 5 BSE images of L-PBF Ti-6Al-4V coupons fabricated using different laser power.

Conclusions

The feasibility of the hardness measurement technique to correlate the defect contents as well as to estimate the process window for L-PBF Ti-6Al-4V material was studied. Throughout this study, the following conclusions were drawn:

1. Hardness was in good correlation with the defect content in the material. The hardness was observed to decrease with an increase in the defect content and vice versa.
2. The rate of decrease in the hardness was higher for underheated coupons as compared to the overheated ones for the same percentage change in the laser power.
3. The martensitic microstructure of the as-built L-PBF Ti-6Al-4V didn't vary significantly with the change in the laser power.

Acknowledgments

This material is based upon the work partially supported by the National Science Foundation (NSF) under grant # 1919818 and the Federal Aviation Administration (FAA) under grant # FAA-12-C-AM-AU-A2.

References

- [1] A. Yadollahi, N. Shamsaei, Additive manufacturing of fatigue resistant materials: Challenges and opportunities, *Int. J. Fatigue.* 98 (2017) 14–31. <https://doi.org/10.1016/J.IJFATIGUE.2017.01.001>.
- [2] S. Lee, N. Ahmad, K. Corriveau, C. Himel, D.F. Silva, N. Shamsaei, Bending properties of additively manufactured commercially pure titanium (CPTi) limited contact dynamic compression plate (LC-DCP) constructs: Effect of surface treatment, *J. Mech. Behav. Biomed. Mater.* 126 (2022) 105042. <https://doi.org/10.1016/J.JMBBM.2021.105042>.
- [3] M.S. Yasin, A. Soltani-Tehrani, S. Shao, M. Haghshenas, N. Shamsaei, A Comparative Study on Fatigue Performance of Various Additively Manufactured Titanium Alloys-NC-

- ND license (<https://creativecommons.org/licenses/by-nc-nd/4.0>) Peer-review under responsibility of the scientific committee of the Fatigue Design 2021 Organizers, (2021). www.sciencedirect.com (accessed May 13, 2022).
- [4] A. Soltani-Tehrani, J. Pegues, N. Shamsaei, Fatigue behavior of additively manufactured 17-4 PH stainless steel: The effects of part location and powder re-use, *Addit. Manuf.* 36 (2020) 101398. <https://doi.org/10.1016/j.addma.2020.101398>.
- [5] P.D. Nezhadfar, R. Shrestha, N. Phan, N. Shamsaei, Fatigue data for laser beam powder bed fused 17-4 PH stainless steel specimens in different heat treatment and surface roughness conditions, *Data Br.* 25 (2019) 104215. <https://doi.org/10.1016/j.dib.2019.104215>.
- [6] A. Poudel, N. Shamsaei, S. Shao, Linear elastic finite element calculations of short cracks initiated from the defects : effect of defect shape and size, 2021 *Int. Solid Free. Fabr. Symp.* (2021) 915–922.
- [7] H. Masuo, Y. Tanaka, S. Morokoshi, H. Yagura, T. Uchida, Y. Yamamoto, Y. Murakami, Influence of defects, surface roughness and HIP on the fatigue strength of Ti-6Al-4V manufactured by additive manufacturing, *Int. J. Fatigue.* 117 (2018) 163–179. <https://doi.org/10.1016/j.ijfatigue.2018.07.020>.
- [8] X. Shui, K. Yamanaka, M. Mori, Y. Nagata, K. Kurita, A. Chiba, Effects of post-processing on cyclic fatigue response of a titanium alloy additively manufactured by electron beam melting, *Mater. Sci. Eng. A.* 680 (2017) 239–248. <https://doi.org/10.1016/j.msea.2016.10.059>.
- [9] S. Tammas-Williams, P.J. Withers, I. Todd, P.B. Prangnell, The Effectiveness of Hot Isostatic Pressing for Closing Porosity in Titanium Parts Manufactured by Selective Electron Beam Melting, *Metall. Mater. Trans. A Phys. Metall. Mater. Sci.* 47 (2016) 1939–1946. <https://doi.org/10.1007/s11661-016-3429-3>.
- [10] R. Molaei, A. Fatemi, N. Phan, Significance of hot isostatic pressing (HIP) on multiaxial deformation and fatigue behaviors of additive manufactured Ti-6Al-4V including build orientation and surface roughness effects, *Int. J. Fatigue.* 117 (2018) 352–370. <https://doi.org/10.1016/j.ijfatigue.2018.07.035>.
- [11] R. Ghiaasiaan, A. Poudel, N. Ahmad, P.R. Gradl, S. Shao, N. Shamsaei, High Temperature Tensile and Fatigue Behaviors of Additively Manufactured IN625 and IN718, *Procedia Struct. Integr.* 38 (2022) 581–587. <https://doi.org/10.1016/J.PROSTR.2022.03.059>.
- [12] R. Ghiaasiaan, A. Poudel, N. Ahmad, M. Muhammad, P.R. Gradl, S. Shao, N. Shamsaei, Room Temperature Mechanical Properties of Additively Manufactured Ni-base Superalloys: A Comparative Study, *Procedia Struct. Integr.* 38 (2022) 109–115. <https://doi.org/10.1016/J.PROSTR.2022.03.012>.
- [13] B. Zhang, W.J. Meng, S. Shao, N. Phan, N. Shamsaei, Effect of heat treatments on pore morphology and microstructure of laser additive manufactured parts, *Mater. Des. Process. Commun.* 1 (2019) e29. <https://doi.org/10.1002/mdp2.29>.
- [14] S. Shao, M.J. Mahtabi, N. Shamsaei, S.M. Thompson, Solubility of argon in laser additive manufactured α -titanium under hot isostatic pressing condition, *Comput. Mater. Sci. C* (2017) 209–219. <https://doi.org/10.1016/J.COMMATSCI.2017.01.040>.
- [15] A. Poudel, A. Soltani-Tehrani, S. Shao, N. Shamsaei, Effect of powder characteristics on tensile properties of additively manufactured 17-4 PH stainless steel, 2021 *Int. Solid Free. Fabr. Symp.* (2021).
- [16] H. Gong, K. Rafi, H. Gu, T. Starr, B. Stucker, Analysis of defect generation in Ti–6Al–4V parts made using powder bed fusion additive manufacturing processes, *Addit. Manuf.* 1–4

- (2014) 87–98. <https://doi.org/10.1016/J.ADDMA.2014.08.002>.
- [17] A. du Plessis, Effects of process parameters on porosity in laser powder bed fusion revealed by X-ray tomography, *Addit. Manuf.* 30 (2019) 100871. <https://doi.org/10.1016/j.addma.2019.100871>.
- [18] D.R. Clymer, J. Cagan, J. Beuth, Power–Velocity Process Design Charts for Powder Bed Additive Manufacturing, *J. Mech. Des.* 139 (2017). <https://doi.org/10.1115/1.4037302>.
- [19] G. Kasperovich, G., Gussone, J., Haubrich, J., Schulte, D., Requena, Correlation between porosity and processing parameters in TiAl6V4 produced by selective laser melting, *Mater. Des.* 105 (2016) 160–170.
- [20] N. Sanaei, A. Fatemi, Defects in additive manufactured metals and their effect on fatigue performance: A state-of-the-art review, *Prog. Mater. Sci.* 117 (2021) 100724. <https://doi.org/10.1016/j.pmatsci.2020.100724>.
- [21] WK78911 New Guide for Additive Manufacturing of Metal -- Finished Part Properties -- Methods for Density Measurement, (n.d.). <https://www.astm.org/workitem-wk78911> (accessed May 13, 2022).
- [22] A.B. Spierings, M. Schneider, R. Eggenberger, Comparison of density measurement techniques for additive manufactured metallic parts, (n.d.). <https://doi.org/10.1108/13552541111156504>.
- [23] R. Snell, S. Tammawilliams, L. Chechik, A. Lyle, E. Herna, C. Boig, G. Panoutsos, I. Todd, Methods for Rapid Pore Classification in Metal Additive Manufacturing, *J. Miner. Met. Mater.* 72 (2020). <https://doi.org/10.1007/s11837-019-03761-9>.
- [24] A. du Plessis, I. Yadroitsava, I. Yadroitsev, Effects of defects on mechanical properties in metal additive manufacturing: A review focusing on X-ray tomography insights, *Mater. Des.* 187 (2020) 108385. <https://doi.org/10.1016/j.matdes.2019.108385>.
- [25] D. Maret, N. Telmon, O.A. Peters, B. Lepage, J. Treil, J.M. Inglese, A. Peyre, J.L. Kahn, M. Sixou, Effect of voxel size on the accuracy of 3D reconstructions with cone beam CT, *Dentomaxillofacial Radiol.* 41 (2012) 649. <https://doi.org/10.1259/DMF/81804525>.
- [26] J. Dai, J. Xia, L. Chai, K.L. Murty, N. Guo, M.R. Daymond, Correlation of microstructural, textural characteristics and hardness of Ti–6Al–4V sheet β -cooled at different rates, *J. Mater. Sci.* 55 (2020) 8346–8362. <https://doi.org/10.1007/S10853-020-04603-9/TABLES/3>.
- [27] A.M. Khorasani, I. Gibson, U.S. Awan, A. Ghaderi, The effect of SLM process parameters on density, hardness, tensile strength and surface quality of Ti-6Al-4V, *Addit. Manuf.* 25 (2019) 176–186. <https://doi.org/10.1016/J.ADDMA.2018.09.002>.
- [28] M. Muhammad, J.W. Pegues, N. Shamsaei, M. Haghshenas, Effect of heat treatments on microstructure/small-scale properties of additive manufactured Ti-6Al-4V, *Int. J. Adv. Manuf. Technol.* 103 (2019) 4161–4172. <https://doi.org/10.1007/s00170-019-03789-w>.
- [29] M. Muhammad, M. Masoomi, B. Torries, N. Shamsaei, M. Haghshenas, Depth-sensing time-dependent response of additively manufactured Ti-6Al-4V alloy, *Addit. Manuf.* 24 (2018) 37–46. <https://doi.org/10.1016/J.ADDMA.2018.09.008>.
- [30] Standard Test Method for Analysis of Titanium and Titanium Alloys by Direct Current Plasma and Inductively Coupled Plasma Atomic Emission Spectrometry (Performance-Based Test Methodology), (n.d.). <https://www.astm.org/e2371-21a.html> (accessed June 21, 2022).
- [31] Standard Test Methods for Rockwell Hardness of Metallic Materials, ASTM E18-20, (n.d.). <https://www.astm.org/e0018-19.html> (accessed May 12, 2022).

- [32] Object Research Systems (ORS) Inc, Dragonfly, (2021). <http://www.theobjects.com/dragonfly>.
- [33] C.A. Schneider, W.S. Rasband, K.W. Eliceiri, NIH Image to ImageJ: 25 years of image analysis, *Nat. Methods* 2012 97. 9 (2012) 671–675. <https://doi.org/10.1038/nmeth.2089>.